Molecular Simulations for Understanding the Stabilization of Fullerenes in Water

Kendra Noneman
Micron School of Materials Science
and Engineering
Boise State University
Boise, ID
kendranoneman@u.boisestate.edu

Christopher Muhich
School for Engineering of Matter,
Transport, and Energy
Arizona State University
Tempe, AZ

Kevin Ausman
Department of Chemistry
Boise State University
Boise, ID

Mike Henry
Micron School of Materials Science
and Engineering
Boise State University
Boise, ID

Eric Jankowski
Micron School of Materials Science
and Engineering
Boise State University
Boise, ID
ericjankowski@boisestate.edu

ABSTRACT

Making materials out of buckminsterfullerene is challenging, because it requires first dispersing the molecules in a solvent, and then getting the molecules to assemble in the desired arrangements. In this computational work, we focus on the dispersion challenge: How can we conveniently solubilize buckminsterfullerene? Water is a desirable solvent because of its ubiquity and biocompatibility, but its polarity makes the dispersion of nonpolar fullerenes challenging. We perform molecular dynamics simulations of fullerenes in the presence of fullerene oxides in implicit water to elucidate the role of interactions (van der Waals and Coulombic) on the self-assembly and structure of these aqueous mixtures. Seven coarse-grained fullerene models are characterized over a range of temperatures and interaction strengths using HOOMD-Blue on high performance computing clusters. We find that dispersions of fullerenes stabilized by fullerene oxides are observable in models where the net attraction among fullerenes is about 1.5 times larger than the attractions between oxide molecules. We demonstrate that simplified models are sufficient for qualitatively modeling micellization of these fullerenes and provide an efficient starting point for investigating how structural details and phase behavior depend upon the inclusion of more detailed physics.

KEYWORDS

Self assembly, Computer simulation, GPUs, Molecular dynamics, Undergraduate research, Blue Waters

1 INTRODUCTION

Buckminsterfullerene (C_{60}) can be dispersed in water, starting from both pure solid and organic solutions, rendering this colloid the

most environmentally relevant form of the fullerenes [1–7]. The ability to disperse C_{60} colloids in water, termed "nC_{60}", is of interest from a nanomanufacturing perspective, because such solutions offer a starting point for using thermodynamics to self-assemble nanostructures from these organic conducting building blocks without the need for volatile solvents. Early reports of C_{60} cytotoxicity were followed by substantively conflicting reports of the material's environmental and biological behavior [2, 8–17]. This controversy has elevated C_{60} to a status as a touchstone nanoparticle, in many ways serving as a proxy for the scientific community's responsible development of nanomaterials as an industry.

Since its first laboratory synthesis in 1994 [5], several aspects of nC_{60}'s structure, stability, and reactivity have defied explanation. Of the reported nC_{60} laboratory synthesis methods, most involve transfer of the fullerene material from an organic solvent into water [1, 2, 6, 18–20]. One approach, however, known as AQU/nC_{60}, involves simple extended stirring in water for a period of days to months [6, 7, 19, 21, 22]. This last technique is notoriously inconsistent and unreliable, despite it being the most environmentally-relevant approach. Most critically, the surface chemistry of the colloidal particles must be charged or hydrophilic, or both, in order to render the particles water-stable. The most significant breakthrough in understanding the nature of this surface chemistry came in 2012 with the observation that for AQU/nC_{60} this hydrophilic chemistry results from an unusually-stable epoxide derivative of C_{60}, which is formed through reaction of trace levels of atmospheric ozone with buckminsterfullerene [23]. This same $C_{60}O$ derivative has been shown, at least in some samples, to stabilize aqueous colloidal aggregates of C_{60} (nC_{60}) in three of the main organic solvent-based synthesis techniques: the exchange methods of hexane/isopropyl alcohol/water (HIPA), tetrahydrofuran/water (THF), and toluene/tetrahydrofuran/acetone/water (TTA) [20]. The present work aims to elucidate the self-assembly of fullerenes into colloidal particles under conditions where a mixture of C_{60} and $C_{60}O$ are present. This initial work explores equimolar quantities of each, aiming to understand the minimal physics required to describe colloidal stabilization of C_{60} and $C_{60}O$ in water. What C_{60} and

$C_{60}O$ characteristics and conditions are sufficient for $C_{60}O$ to stabilize micelles (Figure 1) of C_{60}? Are there other thermodynamically stable arrangements of C_{60} and $C_{60}O$?

We approach these questions of fullerene stability through the lens of molecular simulations and micelle self-assembly. Molecular dynamics (MD) and Monte Carlo (MC) simulations have been employed to investigate how the properties of amphiphilic molecules can self-assemble into higher-ordered structures including micelles [24–27]. These simulations provide a convenient way to study how the thermodynamic stability of micelles and bilayers depends on interactions and geometric constraints, as predicted by Israelachvili, Mitchell, and Ninham [28]. For example, MD simulations of model surfactants in a solvent show that micelles of varying structure (disk, cylindrical, and spherical) can readily self-assemble over simulation timescales [26]. More recent work using a more complex MARTINI model of surfactants in water demonstrates that the long timescales of lipid bilayer transformations can be accessed in MD simulations [25]. Representing solvent molecules implicitly using Langevin or Brownian dynamics is another technique for accessing longer timescales, and the work of Noguchi et al. demonstrates that micelles can self-assemble from amphiphilic molecules and aggregate into vesicles in the right conditions [24]. The thermodynamic stability of spherical micelles, cylindrical micelles, vesicles, and bilayers was demonstrated to be a function of amphiphile shape (here, dumbbell size ratio) in MC simulations by Avvisati et al. [27]. In summary, simplified models of amphiphiles have been successfully deployed to study thermodynamic phase behavior and self-assembly for a wide variety of amphiphilic molecules. Here, our coarse model of amphiphilic $C_{60}O$ is developed in the spirit of Refs. [27] and [24] and we investigate its self assembly with C_{60} in an implicit solvent with MD simulations.

2 MODEL

We use MD simulations to investigate a sequence of seven coarse-grained models of C_{60} and $C_{60}O$ to determine how our choice of model determines the structures that self-assemble. In all of the models, C_{60} is represented by a single coarse-grained simulation element (Figure 2(h)), $C_{60}O$ is represented by two spherical simulation elements (Figure 2(a–g)), and water is modeled implicitly using Langevin dynamics [24, 29]. The hydrodynamic drag on each spherical simulation element is described by the Stokes formula

$$F_d = 3\pi\eta d\vec{v} \qquad (1)$$

where η is the viscosity of the fluid, d is the particle diameter, and $\vec{v}$ is the particle velocity. Random forces on each spherical simulation element from the implicit solvent are described by $\zeta(t)$, which is related to the drag force through the fluctuation dissipation theorem

$$\left\langle \zeta(t)^2 \right\rangle = 2F_d T \qquad (2)$$

and where $\langle \zeta(t)\zeta(t') \rangle = 0$. The net effect of modeling the solvent implicitly through Langevin dynamics is that the simulation elements are thermostatted not to travel so fast as to be numerically unstable, but with dynamics and computational cost sufficient to reach equilibration in minutes to hours. We also note that the inertial terms (masses, moments of inertia) do not factor into the equilibrium structures sampled.
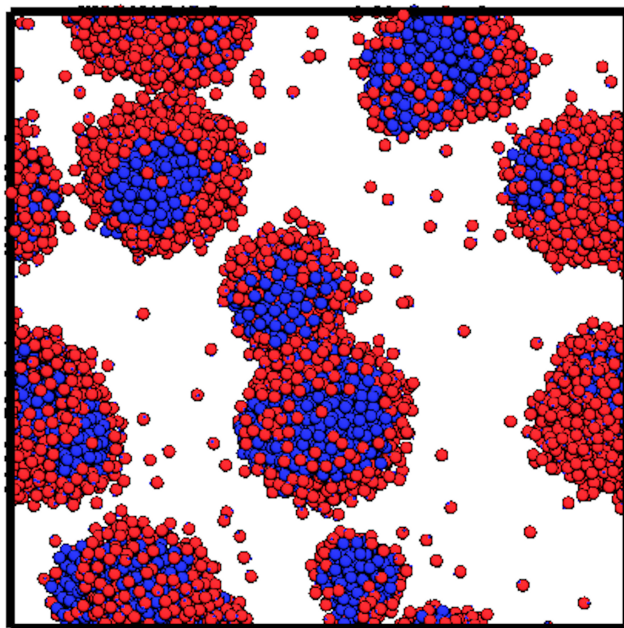
Figure 1: Representative snapshot of C_{60} (blue spheres) stabilized in water with $C_{60}O$ (red spheres with small blue dots) acting as a surfactant between the nonpolar C_{60} and polar water.

The seven models we consider here are chosen to answer: *What combinations of van der Waals interaction strengths, partial charges, and molecular geometry are sufficient to predict the formation of C_{60} micelles stabilized by $C_{60}O$?* The models also roughly represent a gradient of increasing complexity, from simplified models that do not explicitly include long-range electrostatics, to models that have partial charges and moments of inertia informed by first-principles calculations.

(1) The geometry of $C_{60}O$ in Model 1 (Figure 2a) is designed using approximate atomic sizes and positions from the optimized OPLS-AA force field (optimized potentials for the simulation of liquids, all atom) [30].

(2) The geometry of $C_{60}O$ in Model 2 (Figure 2b) is informed by density-functional theory (DFT) calculations described later in this paper.

(3) Model 3 (Figure 2c) uses the same geometry as Model 2, but adds naïve partial charges to the coarse-grained C_{60} and O beads, creating a static dipole across the $C_{60}O$ molecule. Model 3 also scales down the energies of the O-O and O-C_{60} interactions.

(4) Model 4 (Figure 2d) improves upon Model 3 by applying partial charges calculated from first principles and using interaction energies scaled to the represent accurate van der Waals forces.

(5) Model 5 (Figure 2e) is identical to Model 4, except the charge magnitudes are scaled down so the dipole moment on $C_{60}O$ has the correct magnitude, in exchange for lower partial charges.
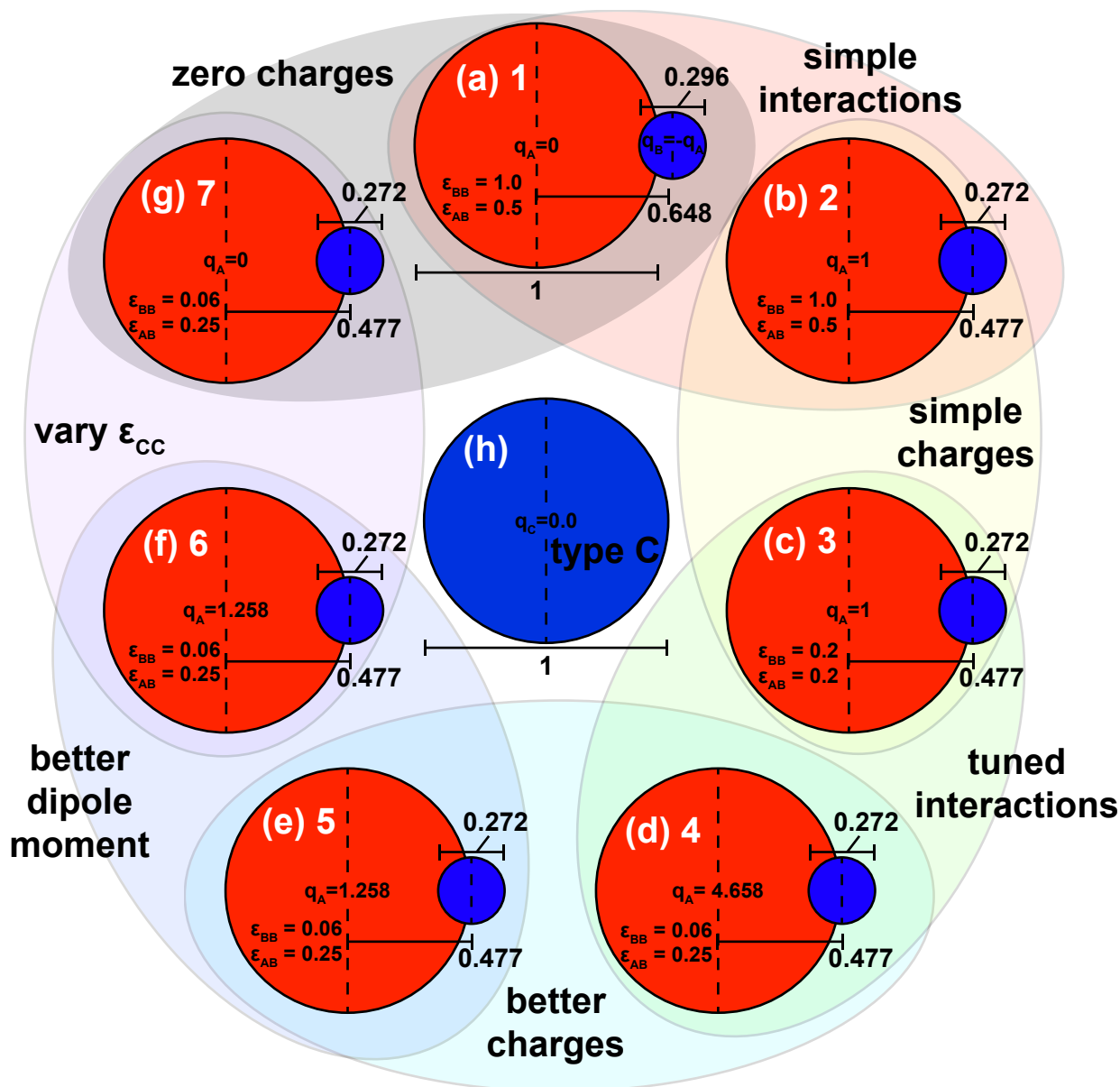
Figure 2: Seven models of $C_{60}O$ are tested for their self-assembly properties with C_{60} (center) in implicit solvent. Clockwise from the top, each successive model is a perturbation to the prior one: Model 2 updates the location and size of the O-group and adds naïve charges to Model 1. Model 3 has more accurate Lennard-Jones (LJ) interaction energies. Model 4 has partial charges informed by density-functionary theory (DFT) calculations and LJ interactions drawn from literature. Model 5 scales the charge magnitudes of Model 4 to have an accurate dipole moment. In Model 6 we keep the Model 5 C_{60} details, but vary ε_{CC}. Model 7 is identical to Model 6 (ε_{CC} varied), but omits partial charges.

(6) Model 6 (Figure 2f) takes a different view and explores how the C_{60}-C_{60} interactions influence phase behavior (by varying ε_{CC}), using the same $C_{60}O$ model as Model 5.

(7) Model 7 (Figure 2g) is identical to Model 6, except it omits the partial charges on $C_{60}O$.

In concert, these models comprise a sequence of assumptions about how C_{60} and $C_{60}O$ behave that begins simply, adds in electrostatics, more accurate van der Waals forces, more accurate charges, and dipoles that enable systematic evaluation of which features are necessary for capturing hypothesized C_{60}-$C_{60}O$ phase behavior.

The potential energy between a pair of simulation elements is described by the Lennard-Jones interaction potential

$$U_{LJ}(r_{ij}) = 4\varepsilon_{kl}\left(\left(\frac{\sigma_{ij}}{r_{ij}}\right)^{12} - \left(\frac{\sigma_{ij}}{r_{ij}}\right)^{6}\right), \qquad (3)$$

where r_{ij} is the center-to-center distance between particles i and j, ε_{kl} is the Lennard-Jones well depth, σ_{kl} is the Lennard-Jones length scale, where k and l indicate particle types, with $k \in \{A, B, C\}$ and $l \in \{A, B, C\}$ in this work. We use Lorentz-Berthelot mixing rules where $\sigma_{kl} = \frac{\sigma_{kk}+\sigma_{ll}}{2}$ represents the sum of the radii of particles i and j whose types are k and l, respectively, and cross-interactions of energy scales are ($\varepsilon_{kl} = \sqrt{\varepsilon_{kk}\varepsilon_{ll}}$) [31, 32]. Equation 3 has a global minimum at $U_{LJ}(r_{ij} = \sigma_{kl}2^{1/6}) = \varepsilon_{kl}$, so we may select ε_{kl} to represent qualitative attractions between model elements A (C_{60} in $C_{60}O$, red elements in Figure 2), B (O, smaller blue elements in Figure 2), and C (C_{60}, Figure 2h).

To minimize confusion that arises when mentally converting between "particle type", "atom types", and "molecules", we henceforth adopt the following naming conventions:

- "A", "B", and "C" are used to refer to the spherical simulation elements that are used to models of $C_{60}O$ and C_{60}, and will only be used in the context of parameters describing interactions between simulation elements (e.g. ε_{BB} and q_A in Table 1) and structural metrics such as radial distribution functions between particles of type B g_{BB}.

- The symbols $C_{60}O$ and C_{60} are used to refer to molecules of $C_{60}O$ and C_{60} generically, both within and outside the context of the models presented here.

- In structural analysis, "A" and $C_{60}O$ are interchangeable, and "C" and C_{60} are interchangeable. That is, a shortcut heuristic for this work is that "A" = $C_{60}O$ and "C" = C_{60}, and we include both sets of symbols as a reminder of the distinction between model implementation ("A", "B", and "C") and molecules (C_{60} and $C_{60}O$).

To minimize unit conversion errors and maximize the interpretability of predictions with other simulation results, we employ base units of mass $M = 1.20 \times 10^{-24}$ kg, length $\sigma = 1.01 \times 10^{-9}$ m, and energy $\varepsilon = 3.24 \times 10^{-20}$ J to convert between physical fullerene parameters and near-unity dimensionless simulation parameters. That is, when we report $\varepsilon_{AB} = 0.5$, it means that $\varepsilon_{AB} = 0.5\varepsilon = 1.62 \times 10-20$ J. Using dimensionless simulation parameters allows for quick inspection of relative magnitudes and aids with analysis. The base units of mass M and length σ correspond to the mass and van der Waals diameter [30] of C_{60}, respectively. The base unit of energy ε corresponds to the minimum potential energy of a C_{60} dimer in water and is within the range of calculations from prior work (2.7×10^{-20} to 3.7×10^{-20}) [33, 34]. Derived units of time $\tau = \sqrt{\frac{M\sigma^2}{\varepsilon}}$ are 6.15×10^{-12} s. One quirk of dimensionless simulation units is the convention of reporting temperatures T in terms of dimensionless energy, which can be converted to Kelvin using $T_{Kelvin} = \frac{\varepsilon T}{k_B}$, where $k_B = 1.38 \times 10^{-23}$ J/K. With $\varepsilon = 3.24 \times 10^{-20}$ J, $T = 1$ corresponds to 2348 K, but we caution overinterpretation of this absolute temperature: Rather, we are reminded that constructing a model in terms of ε—a coarse-grained aqueous C_{60} interaction, whatever it may be—we are able to investigate what other model parameters are

Table 1: Interaction parameters representing oxygen-oxygen ε_{BB}, functionalized C_{60}-oxygen ε_{AB}, and unfunctionalized C_{60}-C_{60} attractions, as well as partial charges on functionalized C_{60} (q_A) and O (q_B) groups.

Model	ε_{BB}	ε_{AB}	ε_{CC}	q_A	q_B
1	1	0.5	1	0	0
2	1	0.5	1	1	-1
3	0.2	0.2	1	1	-1
4	0.06	0.25	1	4.658	-4.658
5	0.06	0.25	1	1.257	-1.257
6	0.06	0.25	1.0 to 2.0	1.257	-1.257
7	0.06	0.25	1.0 to 2.0	0	0

sufficient for observing micellization. Framed this way, correspondence of room-temperature (298 K) micellization in experiments with the present model's predictions at $T = 0.7$ would provide rationale for re-interpreting $\varepsilon = \frac{298 \text{ K} \times 1.38 \times 10^{-23} \text{ J/K}}{0.7} = 5.87 \times 10^{-21}$ J within the context of this model.

The $C_{60}O$ are represented as rigid bodies [35]. This minimal model allows for the shapes of these molecules to be realistically represented without having to keep track of their computationally expensive internal degrees of freedom. We choose interaction strengths (ε_{AA}, ε_{BB}, and ε_{CC}) in terms of ε to systematically model systems with varying degrees of attraction. In this work, we focus on understanding how the choice of ε_{kl}'s determines the structures that emerge (Table 1).

2.1 Partial Charge Calculation

To determine charge distribution on the fullerene and the position of the oxide oxygen (Models 4, 5, 6, and 7), we employ quantum chemical calculations using density-functional theory (DFT). The calculations are carried out using Quantum Espresso [36] with periodic boundary conditions using the Perdew-Burke-Ernzerhof (PBE) generalized gradient approximation (GGA) exchange-correlation functional [37]. Projector augmented wave (PAW) pseudopotentials [38] enable explicit calculation of the 2s and 2p electrons of C and O. Calculations are conducted at the Γ point. C_{60} is initialized in large cube with edges greater than 20Å (roughly three times the diameter of the fullerene), so as to minimize periodic image interactions.

The wave functions are composed of summations of plane waves with energies up to 45 Rydberg (612 eV). No differences in geometry or energies were seen between the calculation using a 45 Ry cutoff energy and a calculation using a 40 Ry cutoff energy, suggesting that both cutoff energies are sufficient to accurately model the wave function. As both wave functions are calculated to ensure convergence, we used the more accurate 45 Ry wave function for all further analysis. Bader analysis [39] is used to determine the charge on the atoms in the Buckyball. The code used to calculate the Bader charges was written by the Henkelman group [40, 41].

3 METHODS

Coarse-grained molecular dynamics simulations are performed using the HOOMD-Blue simulation engine [42] on NVIDIA K20 GPUs

on the NCSA Blue Waters and Boise State Kestrel computing clusters. Each simulation is performed using a single K20 GPU, during which the potential energy and simulation snapshots of the particles are logged. Simulations are performed in the canonical (constant number of particles N, volume V, and temperature T) ensemble using the Nosé-Hoover thermostat [43] and the MTK equations [44, 45]. Quaternions are used to represent the orientational degrees of freedom of the $C_{60}O$ molecules. Long-range electrostatics are calculated using the particle-particle particle-mesh (PPPM) method [46]. Positions and quaternions are updated via the velocity Verlet integration of Newton's equations of motion after every dimensionless time step, $dt = 0.001\tau$ [47].

Simulation volumes are initialized on a square lattice with constant number density $\eta = 0.074$ and equal amounts of C_{60} and $C_{60}O$ in a cubic volume. Small debugging jobs are performed with 150 each of C_{60} and $C_{60}O$, and the largest jobs are performed with 8,000 of each. Simulation snapshots presented in the figures here are from production jobs with 3,375 each of C_{60} and $C_{60}O$, for 10,125 total simulation elements. We consider systems to be equilibrated once the potential energy reaches a stable average, which for the coldest systems studied here occurs after about 2×10^7 time steps in the largest system sizes, and in under 4×10^6 steps for production runs (Figure 3). After equilibration is achieved, we average statistically-independent samples (over 20 for all systems studied here), requiring 1×10^7 steps for the largest systems and 1×10^6 for the production systems. Simulation snapshots are visualized using Visual Molecular Dynamics (VMD) [48], and plotting of simulation data (potential energy trajectories and radial distribution functions $g(r)$) are performed with matplotlib [49].

We use $g_{i,j}(r)$ to measure local spatial correlations between particle types i and j and to distinguish between "dispersed", "aggregate-onset", "fluid clusters", "solid clusters", and "micelle" structures (Figure 4 and Figure 5). The key $g(r)$ metrics we focus on here are peaks corresponding to first- ($r = 1.15\sigma$) and second-nearest neighbor ($1.85\sigma < r < 2.3\sigma$) distances, and whether $g(r)$ converges to the system density at large separations ($\lim_{r \to 6} g(r) = 1$). The magnitude of the first-nearest neighbor peak is used to indicate relative contact frequencies, and a peak at $r = 1.15\sigma$ is expected, because the global minimum of Equation 3 occurs at $r = 1.12\sigma$, and the C_{60} simulation elements have the small oxide component that contributes slightly to average separations. The second-nearest neighbor peak is used to distinguish fluid clusters from dispersed systems. If $\lim_{r \to 6} g(r) > 1$, we expect to find tightly-packed clusters that do not uniformly fill the simulation volume. In micelle cases we use $g_{AC}(r)$ to quantify how "tightly" the shell covers the core of the micelle.

4 RESULTS AND DISCUSSION

We perform MD simulations of equimolar C_{60} and $C_{60}O$ in implicit solvent for seven models. For each model, we vary temperature T to observe transitions between phases. In Models 6 and 7, we vary temperature T and C_{60}-C_{60} interactions (ε_{CC}). After equilibration, simulation snapshots and radial distribution functions $g(r)$ are generated from representative microstates. In this section we present, interpret, and compare the transitions and structures for the seven
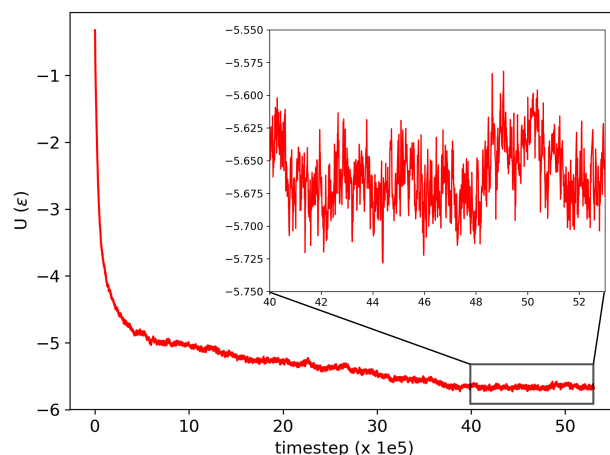
Figure 3: Per-molecule potential energy trajectory for a representative slow-to-relax simulation (Model 7, $T = 0.7$ $\varepsilon_{CC} = 1.5$) that reaches equilibration after 4 million steps and is then sampled fluctuating about a stable average for 1.3 million steps. Inset: Detail of equilibrium potential energy fluctuations.
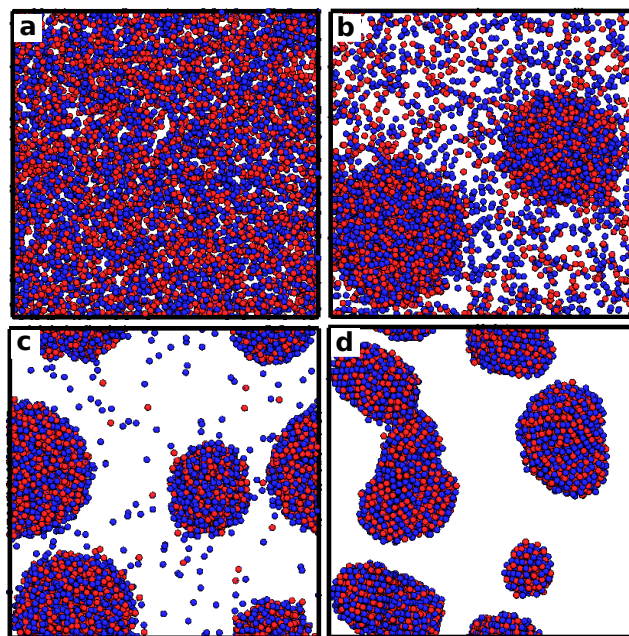
Figure 4: We observe that all seven models transition between the following four phases as temperature is decreased: (a) Dispersed: Molecules move freely and aggregate minimally, (b) Aggregate-onset: Formation of at least one region of relatively high molecular density, (c) Fluid clusters: Few un-aggregated molecules, but molecules still move freely within the clusters, and (d) Solid-like clusters: Rigid clusters where molecules vibrate about static positions within the aggregate.
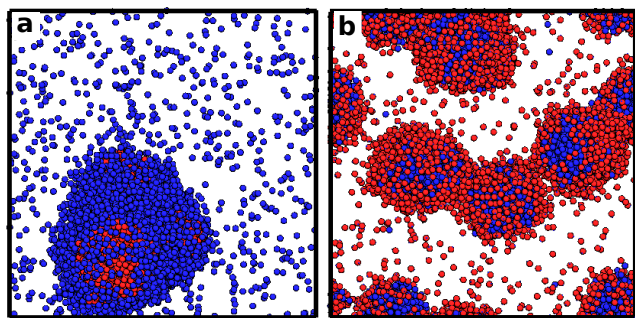
Figure 5: The "micelle" structures observed here are characterized by thin layers of one type of molecule encapsulating spherical clusters of the other molecule type. Here we observe both (a) micelles in which C_{60} encapsulates $C_{60}O$ (Model 4, $T = 0.7$), and (b) micelles in which $C_{60}O$ encapsulates C_{60} (Model 7, $T = 0.7$). Micelle stability is not observed for all models. When micelles are observed, it is at temperatures below aggregate-onset and only for sufficiently high attraction between C_{60} molecules (ε_{CC}).

Figure 6: Measurements of spatial correlations of simulation elements and representative snapshots at $T = 1.0$ for a) Model 1, b) Model 2, c) Model 3, and d) Model 5. At this temperature, aggregation is observed in Models 1 and 2 but not Models 3 and 5. Red g_{AA} measures correlations between the fullerene cages of $C_{60}O$, which are rendered as red spheres. Dashed purple g_{AC} measures correlations between C_{60}'s and the fullerene cages of $C_{60}O$. Dotted blue g_{CC} measures correlations between C_{60}, which are rendered as blue spheres.

models. The results presented here are for the production simulations of 10,125 simulation elements representing 3,375 C_{60} and 3,375 $C_{60}O$ molecules. Overall, we observe the same sequence of structural transitions as we decrease temperature: from dispersed, to aggregate-onset, then fluid, and finally solid-like (Figure 4). For a subset of models, micelles are observed to self-assemble below the aggregate-onset temperature.

(1) In Model 1, fluid clusters emerge between $T = 1.3$ and $T = 1.2$. Aggregation increases (as measured by $g(r = 1.15)$) for all simulation element types (AA followed by AC followed by CC) as temperature is lowered from $T = 1.2$ to $T = 0.7$. A crystallization transition is observed at $T = 0.6$.

(2) Model 2 adds charges relative to Model 1, and we observe the same behaviors as in Model 1 but with fewer, larger clusters (Figure 6b).

(3) Decreasing ε_{BB} in Model 3 causes phase transitions to occur at lower temperatures ($T = 0.9$ for fluid clusters, $T = 0.4$ for solid clusters), but the observed structures are the same as in Models 1 and 2. This is expected, because the thermodynamic driver for oxygen aggregation is smaller ($\varepsilon_{BB} = 0.2$ vs $\varepsilon_{BB} = 1.0$).

(4) Observations of Model 4 differ significantly from Models 1–3, and the model differs in the utilization of partial charges informed by DFT calculations and LJ interactions ($q_A = 4.658$ and $\varepsilon_{AB} = 0.25$). Stronger $C_{60}O$ fullerene cage (AA) aggregation is observed at $T = 1.8$, and shells of C_{60} form around $C_{60}O$ aggregates around $T = 0.9$ (inversions of the experimentally hypothesized micelles, Figure 5(a)). Crystallization occurs at $T = 0.7$.

(5) In Model 5, charge magnitudes are decreased to model a more accurate dipole moment, but the εs from Model 4 are retained. We observe fluid clusters at $T = 0.9$ and solid clusters at $T = 0.5$, but overall observations follow models 1–3: mixed fluid and solid clusters.

(6) Within Model 6 we vary ε_{CC} from 1.0 to 2.0 over $0.6 \leq T \leq 1.0$. Higher values of ε_{CC} promote C_{60}-C_{60} aggregation. Within these ranges of T and ε_{CC} we observe micelles of $C_{60}O$ around C_{60}. (Fig. 5(b))

(7) Within Model 7 we also vary ε_{CC} from 1.0 to 2.0 over $0.6 \leq T \leq 1.0$, but without any long-range electrostatics. Shells of $C_{60}O$ around C_{60} still begin to form, but the aggregates have slightly different structures without the charges.

In summary, Models 6 and 7 are sufficient to observe the experimentally hypothesized micelle stabilization of $C_{60}O$ monolayers forming around spherical clusters of C_{60} in solution. The only difference between these two models is the presence of electrostatic charges in Model 6 that are absent in Model 7. The self-correlations of $C_{60}O$'s and C_{60}'s are measured to be higher in Model 6 (Figure 9), so the presence of charges has measurable impact on local structural details. In both Models 6 and 7, $C_{60}O$ is observed to play the role of micelle surfactant around clusters of C_{60} when $\varepsilon_{CC} \geq 1.5$.

4.1 Models 1, 2, 3, and 5

The structures observed in Models 1, 2, 3, and 5 are very similar. At colder temperatures, $C_{60}O$'s and C_{60}'s aggregate, but they do not demonstrate thermodynamic preference for spatial segregation by type. Representative snapshots are presented in Figure 6. The major difference between Models 1 and 2 versus 3 and 5 is the temperature at which accumulation begins. Overall, these results indicate that changing charge magnitudes between 0 and 1.3 and varying the oxygen attraction parameter (ε_{BB}) aren't primary facors for micellization (recall Table 1).

4.2   Model 4

Structures observed in Model 4 differ significantly from Models 1-3 and 5. Model 4 has oxygen interactions informed by the OPLS and MARTINI force fields [30]. Because of this, the oxide molecules aggregate strongly at temperatures at and below $T = 1.8$. At temperatures around $T = 0.9$, nearly all of the $C_{60}O$'s have grouped up into one large cluster, but the C_{60}'s remain detached. As the temperature is lowered further, the C_{60}'s begin sticking to the surface of the $C_{60}O$ cluster and form a shell around the outside.
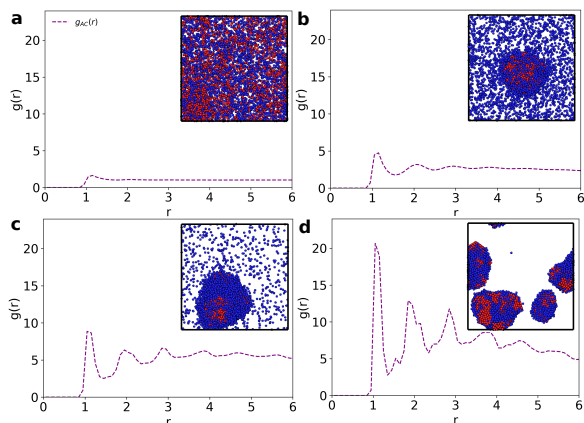
Figure 7: Local structure and representative snapshots from Model 4 at various temperatures. $g_{AA}(r)$ and $g_{CC}(r)$ have been excluded, as the extremely charged $C_{60}O$ molecules ($q_A = 4.658$) are considerably attractive and crystalline. a) $T = 1.8$ aggregation-onset, b) $T = 0.9$ $C_{60}O$'s aggregate into clump and C_{60}'s remain loose, c) $T = 0.7$ C_{60}'s form a shell around the crystalline $C_{60}O$ cluster, and d) $T = 0.4$ tightly packed clusters, but too cold for C_{60}'s and $C_{60}O$'s to reassemble.

4.3   Models 6 and 7

Experimentally-hypothesized micelles of C_{60} surrounded by $C_{60}O$ are observed to self-assemble in Models 6 and 7. These two models are used to explore the role ε_{CC} plays in micellization based on the interaction set of Model 5 with (Model 6) and without (Model 7) charges. Model 6 contains the exact long-range electrostatics of Model 5, while in Model 7 these charges are turned off. For both models, we perform simulations with temperatures ranging from $T = 0.6$ to $T = 1.0$ and ε_{CC} ranging from $\varepsilon_{CC} = 1.0$ to $\varepsilon_{CC} = 2.0$.

We observe significant differences in the structures that are thermodynamically assembled by Models 6 and 7:

(1) $C_{60}O$'s aggregate at higher temperatures and with greater frequency in Model 6 (charged).
(2) The first-nearest neighbor peak magnitudes ($g(r = 1.15)$) for Model 6 are greater than Model 7 at the same temperatures (Figure 8 and 9. The difference in peak magnitudes between $C_{60}O$-$C_{60}O$, $C_{60}O$-C_{60}, and C_{60}-C_{60} is also more spread out for the charged system (Figure 8 and 9). This signifies that charges increase the relative contact frequencies.
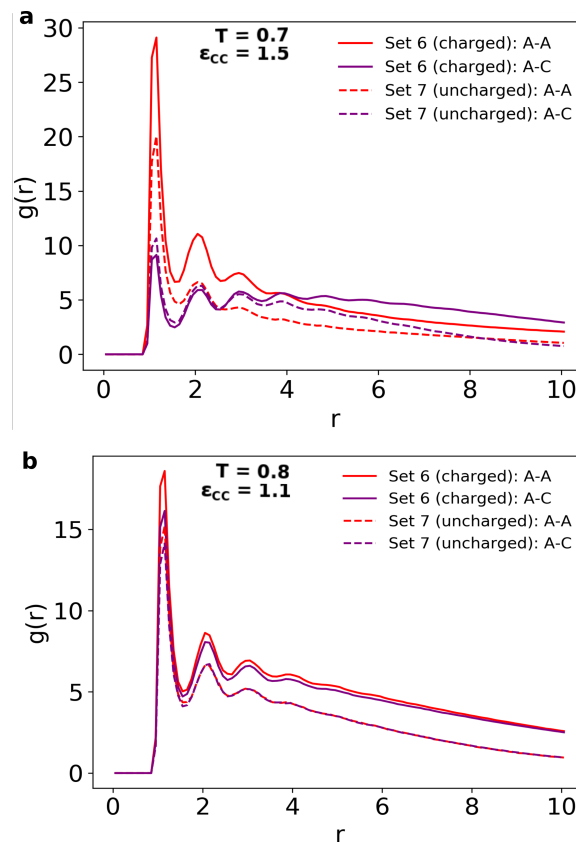
Figure 8: Comparisons of $g_{AA}(r)$ and $g_{AC}(r)$ for the charged Model 6 and uncharged Model 7 show greater oxide aggregation in the charged cases. a) $T = 0.7$ and $\varepsilon_{CC} = 1.5$, **b)** $T = 0.8$ and $\varepsilon_{CC} = 1.1$. **The concave-down shape of** g_{AC} **in solid purple in (a) with a moving average trending up (in this case with a moving average maximum around $g_{AC}(r = 5) = 6$) before turning downwards is an unusual $g(r)$ feature that is representative of micelles with a sheath of either A or C around the other type.**

(3) Lastly, Model 6 (with charged $C_{60}O$'s) consistently has a lower quantity of clusters compared to Model 7 (with uncharged $C_{60}O$'s).

We interpret these observations to indicate that the dipole-dipole interactions available in Model 6 facilitate the aggregation of $C_{60}O$ molecules and enhance the exclusion of C_{60} from $C_{60}O$. In sum, Models 6 and 7 demonstrate that stabilization of C_{60} clusters in water by $C_{60}O$ requires the effective attraction of C_{60} be roughly 50% greater than the net attractions between $C_{60}O$. This 50% heuristic derives from $\varepsilon_{CC} > 1.5$ being required to see micellization, versus $\varepsilon_{AA} = 1$ plus any contributions from BB, AB, and electrostatic interactions (if present). Both models capture qualitative micellization, and the differences between the two models demonstrate that micellization transition temperatures and the structural details of the micelles can be further fine-tuned through the inclusion of detailed electrostatic interactions. To further put these results
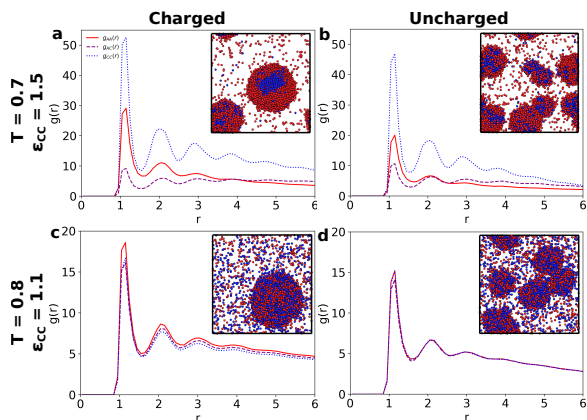
Figure 9: Comparison of Models 6 and 7 for varying temperature and ε_{CC}. a) Model 6: $T = 0.7$ **and** $\varepsilon_{CC} = 1.5$, **b) Model 7:** $T = 0.7$ **and** $\varepsilon_{CC} = 1.5$, **c) Model 6:** $T = 0.8$ **and** $\varepsilon_{CC} = 1.1$, **d) Model 7:** $T = 0.8$ **and** $\varepsilon_{CC} = 1.1$.

into context, we reiterate that all of the observations presented are for *implicit water*: The drag and thermal fluctuations of water are modeled through Equations 1 and 2, and hydrophobic-hydrophilic interactions are implied through the choice of ε and q. These results demonstrate both that (1) micellization of C_{60} by $C_{60}O$ can phenomenalogically be described with a simple model, and (2) the conditions under which micelles form may be more readily deduced by searching parameter space, as performed here, as opposed to performing more expensive (perhaps intractably so) fully-atomistic or first-principles calculations.

5 CONCLUSIONS

Through systematic iteration of minimal models of C_{60} and $C_{60}O$, we have identified sufficient conditions for micelles of $C_{60}O$-sheathed C_{60} to form: When the net attraction between C_{60} molecules is at least 50% larger than the attraction between $C_{60}O$ molecules ($\varepsilon_{CC} > 1.5$), and when solvent thermal fluctuations are low ($T \leq 0.7$) relative to $C_{60}O$-attractions. We also find that including long-range electrostatics and a dipole moment informed by DFT calculations, the fraction of free oxides observed in solution is lower due to their assembly as the surfactant on the micelles. In sum, the minimal models of water presented here (Models 6 and 7) demonstrate fullerene micellization. These models, which equilibrate in minutes on a modern CPU or GPU, can now be used to efficiently probe questions about how micellization depends on interaction parameters beyond the present work.

Connecting the details of these models back to experimental conditions is in theory possible, but not straightforward. Small amounts of dissolved salts, for example, have a strong impact on charge screening and therefore complicate translation between models and experimental conditions. Further, the polarizability of water and fullerene molecules will determine the actual kinetics and thermodynamics of micelle formation. Nevertheless, the models developed here should provide a useful foundation for future studies of fullerene micellization in water. As one example, future studies investigating the role $C_{60}O$ and C_{60} concentrations have

on micelle formation and micelle size are a natural extension of the present work. Microscopy or zeta potential measuremnts that deduce cluster sizes and surfactant ($C_{60}O$) thickness would also provide natural extensions and data for validation of this work. Further calibration of the interaction parameters in Models 6 and 7 can be performed with experimental measurements of colloidal size distributions, and these calibrated models would provide additional capabilities for predicting temperature ranges over which micellization is optimized or thermodynamically unfavorable. We expect the use of simplified models such as the ones presented here to aid in the interpretation of experiments of aqueous fullerene dispersion and ultimately inform more efficient methods for incorporating fullerenes into the advanced materials of the future.

6 REFLECTIONS

Participating in the Blue Waters Student Internship Program in 2016 kick-started my (KN) computational science career and passion for data science. It all started during the two-week petascale institute at the University of Illinois at Urbana-Champaign where I, alongside twenty-five other aspiring computational scientists, learned programming basics and how to submit jobs to a supercomputer, including those comprising the beginnings of this project. We discussed our own projects and brainstormed ideas for improving their effectiveness by employing complex HPC concepts. Through this experience, I also made invaluable networking connections with scientists from both the Shodor Education Foundation and the National Center for Supercomputing Applications. The computing community is close-knit and incredibly supportive, for which I am very grateful to be a part. Working on this project and participating in the Blue Waters program gave me a glimpse at the abundant opportunities available in high-performance computing. Scientists from many different backgrounds (biology, physics, engineering, climatology) attended the institute to develop their skills and advance their respective fields.

The largest challenge in this project was completing and submitting this manuscript! While the basic science was accomplished during the 2016 Blue Waters internship, balancing data analysis, learning scientific writing, and doing scientific writing with classes, varsity track and field, and engineering society involvement caused the submission to be rather delayed. Nevertheless, I am proud of the story we were able to tie together with this work, and the trajectory on which the Blue Waters internship has put me.

My ever-evolving expertise and curiosity in computation have provided me with exposure to projects in materials science, astrochemistry, and even neuroscience. The technical skills, confidence, networking connections, and data-driven mindset I developed during this experience will facilitate my future endeavours; this includes my pursuit of a Ph.D. in Neural Computation at Carnegie Mellon University, which I will begin in the Fall of 2020.

7 SOFTWARE

Job submission scripts and analysis are available in the online supplementary information.

REFERENCES

[1] J. D. Fortner, D. Y. Lyon, C. M. Sayes, A. M. Boyd, J. C. Falkner, E. M. Hotze, L. B. Alemany, Y. J. Tao, W. Guo, K. D. Ausman, V. L. Colvin, and J. B. Hughes. C 60 in Water: Nanocrystal Formation and Microbial Response. *Environmental Science & Technology*, 39(11):4307–4316, jun 2005.

[2] Grigoriy V. Andrievsky, Marina V. Kosevich, Oleh M. Vovk, Vadim S. Shelkovsky, and Lyudmila A. Vashchenko. On the production of an aqueous colloidal solution of fullerenes. *Journal of the Chemical Society, Chemical Communications*, 8(12):1281, 1995.

[3] Shigeru Deguchi, Rossitza G. Alargova, and Kaoru Tsujii. Stable Dispersions of Fullerenes, C60 and C70, in Water: Preparation and Characterization. *Langmuir*, 17(19):6013–6017, sep 2001.

[4] Nikolay O. Mchedlov-Petrossyan, Vladimir K. Klochkov, and Grigoriy V. Andrievsky. Colloidal dispersions of fullerene C60 in water: some properties and regularities of coagulation by electrolytes. *Journal of the Chemical Society, Faraday Transactions*, 93(24):4343–4346, 1997.

[5] Walter A. Scrivens, James M. Tour, Kim E. Creek, and Lucia Pirisi. Synthesis of 14C-Labeled C60, Its Suspension in Water, and Its Uptake by Human Keratinocytes. *Journal of the American Chemical Society*, 116(10):4517–4518, may 1994.

[6] Jonathan A. Brant, Jérôme Labille, Jean-Yves Bottero, and Mark R. Wiesner. Characterizing the Impact of Preparation Method on Fullerene Cluster Structure and Chemistry. *Langmuir*, 22(8):3878–3885, apr 2006.

[7] J. Labille, J. Brant, F. Villiéras, M. Pelletier, A. Thill, A. Masion, M. Wiesner, J. Rose, and J.âĂŘY. Bottero. Affinity of C60 Fullerenes with Water. *Fullerenes, Nanotubes and Carbon Nanostructures*, 14(2-3):307–314, dec 2006.

[8] Alok Dhawan, Julian S. Taurozzi, Alok K. Pandey, Wenqian Shan, Sarah M. Miller, Syed A. Hashsham, and Volodymyr V. Tarabara. Stable Colloidal Dispersions of C60 Fullerenes in Water: Evidence for Genotoxicity. *Environmental Science & Technology*, 40(23):7394–7401, dec 2006.

[9] Najla Gharbi, Monique Pressac, Michelle Hadchouel, Henri Szwarc, Stephen R. Wilson, and Fathi Moussa. [60]Fullerene is a Powerful Antioxidant in Vivo with No Acute or Subacute Toxicity. *Nano Letters*, 5(12):2578–2585, dec 2005.

[10] Nicole Levi, Roy R Hantgan, Mark O Lively, David L Carroll, and Gaddamanugu L Prasad. C60-fullerenes: detection of intracellular photoluminescence and lack of cytotoxic effects. *Journal of Nanobiotechnology*, 4(1):14, 2006.

[11] Delina Y. Lyon and Pedro J.J. Alvarez. Fullerene Water Suspension (nC 60) Exerts Antibacterial Effects via ROS-Independent Protein Oxidation. *Environmental Science & Technology*, 42(21):8127–8132, nov 2008.

[12] Eva Oberdörster. Manufactured Nanomaterials (Fullerenes, C60) Induce Oxidative Stress in the Brain of Juvenile Largemouth Bass. *Environmental Health Perspectives*, 112(10):1058–1062, apr 2004.

[13] Christie M. Sayes, John D. Fortner, Wenh Guo, Delina Lyon, Adina M. Boyd, Kevin D. Ausman, Yizhi J. Tao, Balaji Sitharaman, Lon J. Wilson, Joseph B. Hughes, Jennifer L. West, and Vicki L. Colvin. The Differential Cytotoxicity of Water-Soluble Fullerenes. *Nano Letters*, 4(10):1881–1887, oct 2004.

[14] Christie M. Sayes, Andre M. Gobin, Kevin D. Ausman, Joe Mendez, Jennifer L. West, and Vicki L. Colvin. Nano-C60 cytotoxicity is due to lipid peroxidation. *Biomaterials*, 26(36):7587–7595, dec 2005.

[15] Naohide Shinohara, Takeru Matsumoto, Masashi Gamo, Arisa Miyauchi, Shigehisa Endo, Yoshitaka Yonezawa, and Junko Nakanishi. Is Lipid Peroxidation Induced by the Aqueous Suspension of Fullerene C 60 Nanoparticles in the Brains of Cyprinus carpio ? *Environmental Science & Technology*, 43(3):948–953, feb 2009.

[16] Shiqian Zhu, Eva Oberdörster, and Mary L. Haasch. Toxicity of an engineered nanoparticle (fullerene, C60) in two aquatic species, Daphnia and fathead minnow. *Marine Environmental Research*, 62:S5–S9, jan 2006.

[17] Xiaoshan Zhu, Lin Zhu, Yupeng Lang, and Yongsheng Chen. Oxidative Stress And Growth Inhibition In The Freshwater Fish Carassius Auratus Induced By Chronic Exposure To Sublethal Fullerene Aggregates. *Environmental Toxicology and Chemistry*, 27(9):1979, 2008.

[18] Randall D. Maples, Martha E. Hilburn, Befrika S. Murdianti, Rangika S. Hikkaduwa Koralege, Jason S. Williams, Satish I. Kuriyavar, and Kevin D. Ausman. Optimized solvent-exchange synthesis method for C60 colloidal dispersions. *Journal of Colloid and Interface Science*, 370(1):27–31, mar 2012.

[19] Jonathan Brant, Hélène Lecoanet, Matt Hotze, and Mark Wiesner. Comparison of Electrokinetic Properties of Colloidal Fullerenes (n -C 60) Formed Using Two Procedures âĂ. *Environmental Science & Technology*, 39(17):6343–6351, sep 2005.

[20] Martha E. Hilburn, Befrika S. Murdianti, Randall D. Maples, Jason S. Williams, Joshua T. Damron, Satish I. Kuriyavar, and Kevin D. Ausman. Synthesizing aqueous fullerene colloidal suspensions by new solvent-exchange methods. *Colloids and Surfaces A: Physicochemical and Engineering Aspects*, 401:48–53, may 2012.

[21] Befrika S. Murdianti, Joshua T. Damron, Martha E. Hilburn, Randall D. Maples, Rangika S. Hikkaduwa Koralege, Satish I. Kuriyavar, and Kevin D. Ausman. C60 oxide as a key component of aqueous C60 colloidal suspensions. *Environmental Science and Technology*, 46(14):7446–7453, 2012.

[22] Xuekun Cheng, Amy T. Kan, and Mason B. Tomson. Naphthalene Adsorption and Desorption from Aqueous C 60 Fullerene. *Journal of Chemical & Engineering Data*, 49(3):675–683, may 2004.

[23] Befrika S. Murdianti, Joshua T. Damron, Martha E. Hilburn, Randall D. Maples, Rangika S. Hikkaduwa Koralege, Satish I. Kuriyavar, and Kevin D. Ausman. C 60 Oxide as a Key Component of Aqueous C 60 Colloidal Suspensions. *Environmental Science & Technology*, 46(14):7446–7453, jul 2012.

[24] Hiroshi Noguchi and Masako Takasu. Self-assembly of amphiphiles into vesicles: A Brownian dynamics simulation. *Physical Review E - Statistical Physics, Plasmas, Fluids, and Related Interdisciplinary Topics*, 64(4):7, 2001.

[25] Siewert J. Marrink, Jelger Risselada, and Alan E. Mark. Simulation of gel phase formation and melting in lipid bilayers using a coarse grained model. *Chemistry and Physics of Lipids*, 135(2):223–244, 2005.

[26] Susumu Fujiwara, Takashi Itoh, Masato Hashimoto, and Ritoku Horiuchi. Molecular dynamics simulation of amphiphilic molecules in solution: Micelle formation and dynamic coexistence. *Journal of Chemical Physics*, 130(14), 2009.

[27] Guido Avvisati, Teun Vissers, and Marjolein Dijkstra. Self-Assembly of Patchy Colloidal Dumbbells. pages 1–10, dec 2014.

[28] Jacob N Israelachvili, D John Mitchell, and Barry W Ninham. Theory of self-assembly of hydrocarbon amphiphiles into micelles and bilayers. *Journal of the Chemical Society, Faraday Transactions 2*, 72:1525, 1976.

[29] R Kubo. The fluctuation-dissipation theorem. *Reports on Progress in Physics*, 29(1):306, jan 1966.

[30] Robert C. Rizzo and William L. Jorgensen. OPLS all-atom model for amines: Resolution of the amine hydration problem. *Journal of the American Chemical Society*, 121(11):4827–4836, 1999.

[31] H A Lorentz. Ueber die Anwendung des Satzes vom Virial in der kinetischen Theorie der Gase. *Annalen der Physik*, 248(1):127–136, 1881.

[32] Daniel Berthelot. Sur le mélange des gaz. *Compt. Rendus*, 126:1703–1706, 1898.

[33] Ch. Girard, Ph. Lambin, A. Dereux, and A. A. Lucas. van der Waals attraction between two C60 fullerene molecules and physical adsorption of C60 on graphite and other substrates. *Physical Review B*, 49(16):11425–11432, apr 1994.

[34] Hojin Kim, Dmitry Bedrov, Grant D. Smith, and Salt Lake City. Molecular Dynamics Simulation Study of the Influence of Cluster Geometry on Formation of C 60 Fullerene Clusters in Aqueous Solution. *Journal of Chemical Theory and Computation*, 4(2):335–340, 2008.

[35] Trung Dac Nguyen, Carolyn L Phillips, Joshua a. Anderson, and Sharon C Glotzer. Rigid Body Constraints Realized in Massively-parallel Molecular Dynamics on Graphics Processing Units. *Computer Physics Communications*, 182(11):2307–2313, nov 2011.

[36] P. Giannozzi, S. Baroni, N. Bonini, M. Calandra, R. Car, C. Cavazzoni, D. Ceresoli, G. L. Chiarotti, m. Cococcioni, I. Dabo, A. Dal Corso, S. Fabris, G. Fratesi, S. de Gironcoli, R. Gebauer, U. Gerstmann, C. Gougoussis, A. Kokalj, M. Lazzeri, L. Martin-Samos, N. Marzari, F. Mauri, R. Mazzarello, S. Paolini, A. Pasquarello, L. Paulatto, C. Sbraccia, S. Scandolo, G. Sclauzero, A. P. Seitsonen, A. Smogunov, P. Umari, and R. M. Wentzcovitch. Quantum ESPRESSO: a modular and open-source software project for quantum simulations of materials. 2009.

[37] John P. Perdew, Kieron Burke, and Matthias Ernzerhof. Generalized Gradient Approximation Made Simple. *Physical Review Letters*, 77(18):3865–3868, 1996.

[38] G. Kresse and D. Joubert. From ultrasoft pseudopotentials to the projector augmented-wave method. *Physical Review B*, 59(3):1758–1775, 1999.

[39] Richard F. W. Bader. Atoms in Molecules. In *Encyclopedia of Computational Chemistry*. John Wiley & Sons, Ltd, Chichester, UK, apr 2002.

[40] Graeme Henkelman, Andri Arnaldsson, and Hannes Jónsson. A fast and robust algorithm for Bader decomposition of charge density. *Computational Materials*

Science, 36(3):354–360, 2006.

[41] Edward Sanville, Steven D. Kenny, Roger Smith, and Graeme Henkelman. Improved grid-based algorithm for Bader charge allocation. *Journal of Computational Chemistry*, 28(5):899–908, apr 2007.

[42] Joshua A. Anderson, Jens Glaser, and Sharon C. Glotzer. HOOMD-blue: A Python package for high-performance molecular dynamics and hard particle Monte Carlo simulations. *Computational Materials Science*, 173(October 2019):109363, 2020.

[43] William G. Hoover. Canonical Dynamics: Equilibrium Phase-space Distributions. *Physical Review A*, 31(3):1695–1697, 1985.

[44] A. Denner, S. Dittmaier, M. Roth, and L. H. Wieders. Complete electroweak O(alpha) corrections to charged-current e+e- –> 4fermion processes. *The Journal of Chemical Physics*, 101(5):4177–4189, feb 2005.

[45] J. Cao and G. J. Martyna. Adiabatic path integral molecular dynamics methods. II. Algorithms. *The Journal of Chemical Physics*, 104(5):2028–2035, feb 1996.

[46] David N. Lebard, Benjamin G. Levine, Philipp Mertmann, Stephen A. Barr, Arben Jusufi, Samantha Sanders, Michael L. Klein, Athanassios Z. Panagiotopoulos, A Barr, Arben Jusufi, Samantha Sanders, and L Klein. Self-assembly of coarse-grained ionic surfactants accelerated by graphics processing units. *Soft Matter*, 8(8):2385–2397, 2012.

[47] W. C. Swope, H. C. Andersen, P. H. Berens, and K. R. Wilson. A Computer Simulation Method for the Calculation of Equilibrium Constants for the Formation of Physical Clusters of Molecules: Application to Small Water Clusters. *Journal of Chemical Physics*, 76(1):637–649, 1982.

[48] William Humphrey, Andrew Dalke, and Klaus Schulten. VMD: Visual molecular dynamics. *Journal of Molecular Graphics*, 14(1):33–38, feb 1996.

[49] J D Hunter. Matplotlib: A 2D graphics environment. *Computing In Science & Engineering*, 9(3):90–95, 2007.

[50] John Towns, Timothy Cockerill, Maytal Dahan, Ian Foster, Kelly Gaither, Andrew Grimshaw, Victor Hazlewood, Scott Lathrop, Dave Lifka, Gregory D. Peterson, Ralph Roskies, J. Ray Scott, and Nancy Wilkens-Diehr. XSEDE: Accelerating Scientific Discovery. *Computing in Science & Engineering*, 16(5):62–74, sep 2014.